Solid Freeform Fabrication 2024: Proceedings of the 35th Annual International Solid Freeform Fabrication Symposium – An Additive Manufacturing Conference
Reviewed Paper

INFLUENCE OF CONTOUR OFFSET IN LASER POWDER BED FUSION ON MELT POOL BEHAVIORS, SURFACE ROUGHNESS, AND SUB-SURFACE POROSITY

Alex Kleen[*], Edwin Glaubitz[*], and Joy Gockel[*]

[*]Colorado School of Mines, Golden, CO 80401

Abstract

Surface roughness and porosity have been linked to decreased mechanical performance in laser powder bed fusion (PBF-LB) parts. Prior work has shown that contour laser power and speed influence surface roughness, however, changing these parameters also changes the contour melt pool size and the placement of the contour needs to be considered. Contour offset defines the placement of the contour pass relative to the outer edges of the computer aided design file that has been sliced. Coupons with a range of contour speed, power, and offset values are fabricated in PBF-LB from 316L stainless steel. Dimensional accuracy, surface roughness, and sub-surface porosity are characterized. Contour offset is shown to be a critical parameter to control surface and sub-surface defect structure during the PBF-LB process, which can be used to optimize future process development.

1. Introduction

Laser powder bed fusion (PBF-LB) is an additive manufacturing (AM) technique that utilizes a laser to melt metal powder in layers to form a solid part. After each layer, the print bed is lowered by the specified layer height and a new layer of powder is spread across with a recoater. An inert gas such as argon or nitrogen flows across the build platform during the print process to prevent oxidation and remove condensate [1]. For vertical surfaces, each layer is made up of two types of scans: the bulk and the contour passes. Bulk scans make up the majority of the part and typically consist of straight passes across the inside of the part, sometimes in patterns of stripes or islands, stopping shortly before the edge of the geometry. The scan paths are typically rotated between passes. Bulk scanning is often optimized for build speed in order to rapidly form the inside of the part [2]. Contour passes scan the outer surface of the part and are typically slower than bulk scans, making them more accurate to create a better finish. Several contour passes can be added to improve the printed surface finish of an as-printed part [2], [3], [4], [5]. Additive parts allow for more complicated geometries to be formed when compared to traditional manufacturing, as well as reducing the lead times for parts. PBF-LB can be done with several different metals, most commonly titanium alloys such as Ti-6Al-4V, nickel superalloys, aluminums, and stainless steels [6].

High as-built surface roughness has been shown to reduce fatigue life due to surface defects acting as crack initiation sites. Reducing the roughness leads to the crack initiations being caused by internal defects such as porosity and material inclusions. Altering contour process parameters such as laser speed and laser power have been shown to influence surface roughness [7]. Increasing laser power reduces the roughness, while increasing laser speed increases the roughness. The porosity of the parts can also fluctuate with the power and speed settings. Increasing the amount of energy input into the part can result in larger amounts of keyhole type porosity. Surface roughness has also been shown to depend on whether the surface being examined is a side surface, upskin or downskin surface. Downskin surfaces have a higher roughness typically because the material is being processed over the loose powder bed, and the processing parameters used when

producing these downskins has an effect on the surface quality [8], [9], [10], [11]. Laser incidence angle and the direction of the gas flow can also influence the surface roughness of a part. The laser incidence angle changes melt pool formation, and when further from the center can lead to melt pool extensions, where the melt pool increases size away from the laser [12]. The inert gas that flows across the build plate also affects the properties of parts. When the gas flow is either too high or too low, higher levels of porosity and roughness occur. Metal vapors and spatter can cause defects and rougher surfaces, leading to poor performance. [13]

Adding contour passes to the outside of an AM part has been shown to improve the surface roughness of as-built parts. Changing the speed, power, and offset from the bulk can all add to how the surface roughness and sub-surface porosity are affected. Using multiple contour passes has been shown to further improve the as-built roughness. Changing the contour parameters can change the size and shape of the defects formed, making these settings crucial. Contour offset varies heavily between platforms and research into the outer contour placement is lacking in literature.

While parameters like laser speed and power have been widely studied, contour offset parameters and their influence on the final part have not. By using several different laser speeds and powers, contour offset can be further explored. Investigating how contour offset impacts factors like surface roughness and porosity will allow for parameter sets to be further developed.

2. Materials and Methods

2.1. Machine and Material

All specimens for this experiment were built on a 3D Systems DMP Flex 350 PBF-LB machine from 316L stainless steel. Samples were printed using reclaimed powder processed using a DMP sieving station (DMP-151914), which sieves the powder under an inert atmosphere to remove particles larger than 60 μm. Specimens were printed on removeable supports generated in 3DExpert and removed from the build plate using a pneumatic chisel. 3DExpert is the proprietary software included with the DMP Flex 350 and was used to do the slicing and build prep for this experiment. All samples were printed at a 60 μm layer height and recoated using a flexible recoater. 3D Expert uses two contour passes in addition to the bulk scanning. The inner contour pass is offset the same amount as the bulk, meaning that it runs over the outer edge of the bulk. The bulk was scanned first, then the inner contour, and then the outer contour which is the default behavior. The parameters for the inner contour and bulk scans were kept constant between each sample, which can be found in Table 1.

3D Systems Sv10 LT60 Default Parameter Set			
Scan Type	Contour Offset (μm)	Laser Power (W)	Laser Speed (mm/s)
Bulk	150	300	900
Inner Contour	150	300	800

Table 1: Constant parameter settings

3DExpert defines contour offset as the distance between the contour and the boundary of the model geometry. An increased value of contour offset pushes the contour away from the boundary of the CAD model, and inversely a decreased offset brings the contour closer. Because of this, an increased offset brings the outer contour closer to bulk, and a smaller offset pushes the

contour away from the bulk. Figure 1 shows a schematic of the contour offset within a single layer. The default parameter set used for this experiment had the bulk offset and inner contour as the same value, so the outer edge of the bulk lies in the same place as the inner contour.

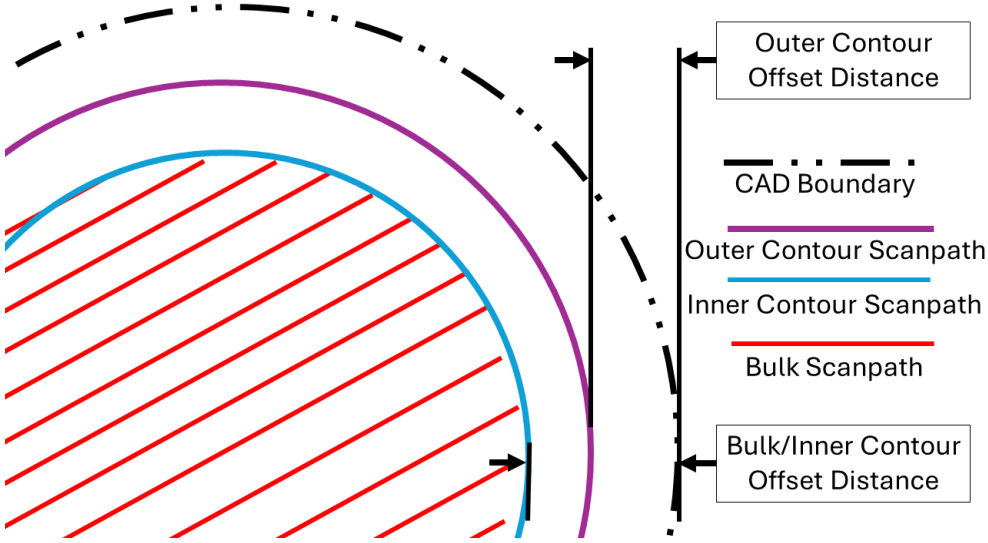

Figure 1: Diagram depicting the scan paths on a layer and the contour offset

To test a variety of different contour offsets and contour melt pool sizes, a combination of five different contour offsets, two different laser power levels, and two different laser speed settings were used. The settings used for each sample can be found below in Table 2.

Outer Contour Scanpath Settings			
Bar Number	Contour Offset (µm)	Laser Power (W)	Laser Speed (mm/s)
41	20	150	250
42	40	150	250
43	63	150	250
44	80	150	250
45	100	150	250
46	20	150	450
47	40	150	450
48	*63*	*150*	*450*
49	80	150	450
50	100	150	450
51	20	115	450
52	40	115	450
53	63	115	450
54	80	115	450
55	100	115	450

Table 2: Processing parameter settings used for outer contour

2.2. Specimen Layout and Geometry

Surface roughness specimens were fabricated as a 5 mm diameter, 15 mm tall cylinder atop a 7 mm cubic base with a 1 mm fillet between the base and the cylinder to provide a smooth transition between the geometries. The 5 mm diameter cylinder was selected because it is within the range of diameter values used for tensile and fatigue testing and the square base was used to provide more precise way to identify the alignment of the sample on the build plate. A numeric label was extruded on one face of the cubic section of the sample. An arrow was engraved on top of the sample to denote the gas flow direction. Each sample has a unique geometry due to the build layout discussed below. The final bar geometry can be found in Figure 2.

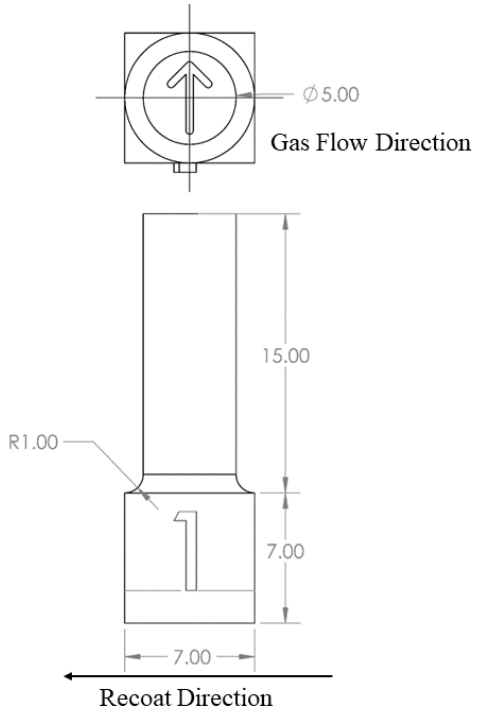

Figure 2: Dimensioned sample geometry

To maintain a consistent laser incident angle, the 15 specimens used were positioned in a circle with a radius of 60 mm/centered on the build plate. Due to the different positions, specimens were rotated so that the label on the side of the bar was facing inwards towards the center. Due to this orientation, the numbered side denoted the laser facing side. This build also included 53 other like bars in a similar layout in different concentric circles for a separate study. This layout was designed to also minimize overlap along the recoating axis which would minimize the influence of recoating defects such as streaking and flicking. The final build layout can be found below in Figure 3. This figure only shows the ring of samples used for this experiment.

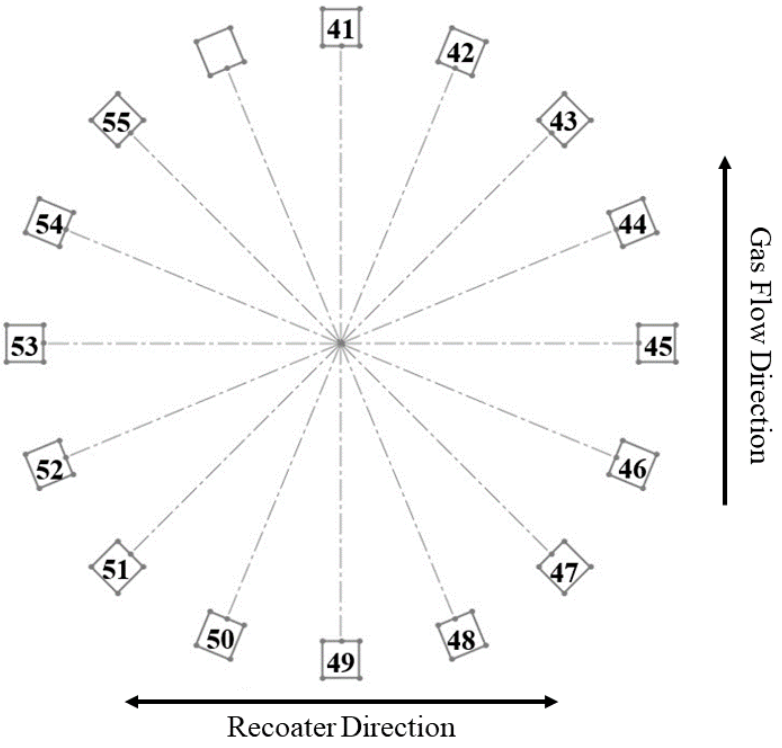

Figure 3: Build layout with numbered specimens with a radius of 60 mm from the center of the platform

2.3. Surface Roughness Characterization

The surface roughness data was gathered using an Olympus OLS-5100 laser confocal scanning microscope (LCSM). Using a 20x long working distance lens, a stitched area of 1.8 mm by 1.8 mm was scanned with a 0.6 µm x-y pixel spacing for each scan on each bar. Each bar was scanned five times on the cylindrical portion of the bar. The first scan was done on side facing the center of the build chamber. The next scan was completed on the side facing away from the gas flow, where the arrow was pointed towards. The subsequent three scans were each rotated 90 degrees from the previous position. The relationship between the gas flow direction and the side facing the center of the build plate changed with each bar, which resulted in some sides getting scanned twice. The relationship between the gas flow direction, laser incident angle, and the bar geometry can be found in Figure 4 in two different orientations to show this changing relationship. Each scan was positioned near the middle of the height of the round bar portion. The raw height data was exported into a csv file for analysis in the commercial surface analysis software OmniSurf3D [14], where the shape (curvature) and noise were filtered and removed. A low pass filter of 5 µm and a high pass filter of 1.8 mm were used remove the noise. A robust Gaussian filter was used instead of the Gaussian filter as it has shown better filtering with the more complicated height profile of these scans.

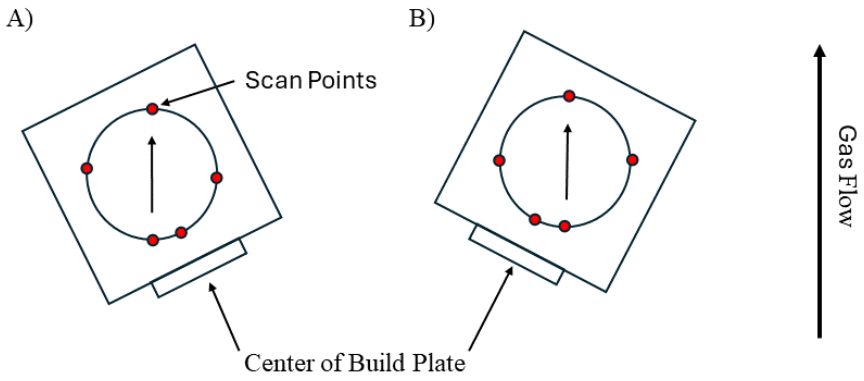

Figure 4: Example surface roughness scanning locations with relation to laser incidence angle and gas flow direction. Figure 4A shows an approximation of sample 55, and Figure 4B shows an approximation of sample 43

OmniSurf3D produced two separate measurement values for the surface roughness of the bars. S_a is the average distance between each point on the surface and the mean plane of every value. This measurement provides a quantitative value for the average roughness of the surface. The equation for S_a can be found in Equation 1 where A is the total area scanned and Z is the measured heights centered on zero.

$$Sa = \frac{1}{A}\iint_A |Z(x,y)|\,dx\,dy$$

Equation 1: Equation to solve for S_a, average roughness

S_v is the measurement of the maximum distance from the mean plane to any point below the mean plane. S_v is helpful as larger S_v values represent larger defects in the surface skin, which have been shown to impact mechanical performance [8]. The equation for S_v is found in Equation 2.

$$Sv = |\min\,(Z(x,y)|$$

Equation 22: Equation to solve for S_v, maximum valley depth

2.4. Material Characterization

The samples were mounted in an Allied Tech Cut saw and cut using a cubic boron nitride metal bonded wafering blade. To get one side of the cut to have half of the bar, a custom mount produced using material extrusion was created. This resulted in the other side of the cut having much less material. The samples were mounted using super glue. The cut was performed along the gas flow direction, as the surface roughness results showed more of a difference in surface roughness dependent on gas flow compared to which side was facing the laser. It was important to have the side being mounted represent as close to half of the bar so that the cross section observed was close to its widest along the cut line. This allowed for the points closest and furthest away

from the gas flow to be analyzed. The side removed during the cut was saved and cleaned in acetone to remove the glue and rinsed with isopropyl alcohol to remove the acetone residue. To separate the sample and the mount, the cut samples were soaked in acetone for 30 minutes while in an ultrasonic cleaner. The samples were then rinsed with isopropyl and water before being mounted in Bakelite.

After being mounted, the samples were polished on a Struers LaboForce-100 autopolisher. The samples were started off at a 320-grit pad and finished with a 1 μm polishing suspension. Intermediate steps of 500 grit, 800 grit, 1000 grit, 9 μm suspension, and 3 μm suspension were used inbetween the steps mentioned above. The samples were cleaned with isopropyl alcohol and water in between each step to prevent cross contamination. To etch the samples, an etchant called glyceregia was used. Glyceregia is a 3:2:1 mixture of glycerol, hydrochloric acid (HCl), and nitric acid (HNO_3). After etching, the samples were rinsed with water and isopropyl alcohol before being capped for protection.

The etched samples were placed in a Keyence VHX-5000 optical microscope. Images were taken from both sides of the sample, as the left side faced towards the gas glow and the right faced away. A subset of the cut bars was imaged using a field emission scanning electron microscope. Images were collected using the secondary electron detector, with a voltage of 20 kV and a working distance of 23 mm. All samples were loaded onto a rotating sample stage so that they could be imaged consecutively with minimal changes in alignment and imaging parameters between samples.

3. Results and Discussion

3.1. Surface Roughness

Figure 5 shows that increasing the melt pool size led to the surface roughness of the samples decreasing. Larger melt pools melt deeper into the part as well as being wider. Therefore, when using the same layer thickness, the deep and wide melt pools create less curvature on the surface and has been shown to improve the surface roughness of an as-built part [8]. Both S_a and S_v, shown in Figure 5A and Figure 5B respectively, decreased as the melt pool size increased. The largest melt pool size led to a tight grouping of S_v, which is a parameter that typically shows higher variance when measured because it is an absolute value. Both the smallest and largest melt pool sizes were shown to have less variability in S_a than the nominal processing parameters.

Figure 6A, which plots the average Sa vs the contour offset distance, shows that there is a correlation between the amount of contour offset and the surface roughness. All three melt pool sizes showed an increase in the measured value of Sa when the contour offset was increased. Figure 6B shows that the average S_v values tended to decrease for the low melt pool size samples as contour offset increased. The nominal processing parameters showed a nonlinear trend between outer contour offset and S_v and did not follow the trend shown in the smaller melt pool size. The S_v values were consistent for the larger melt pool size samples and did not show a relationship between S_v and contour offset.

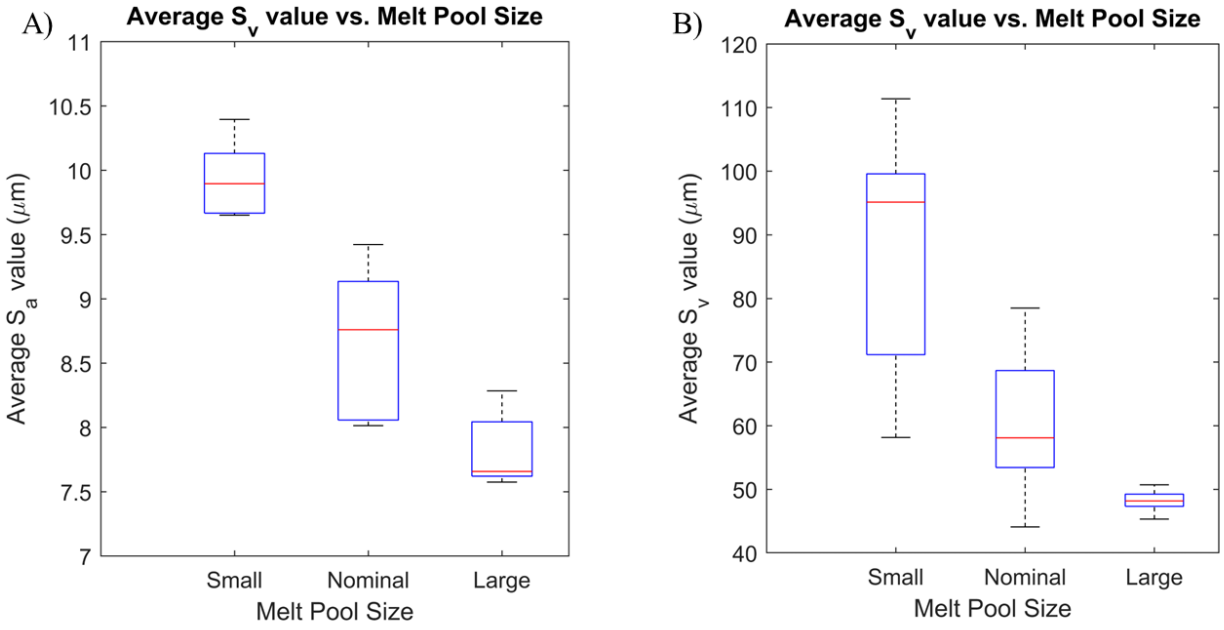

Figure 5: Measured roughness values vs. melt pool size. Figure 5A shows the distribution of the S_a measurements taken vs. melt pool size. Figure 5B shows the distribution of the S_v measurements taken vs. melt pool size.

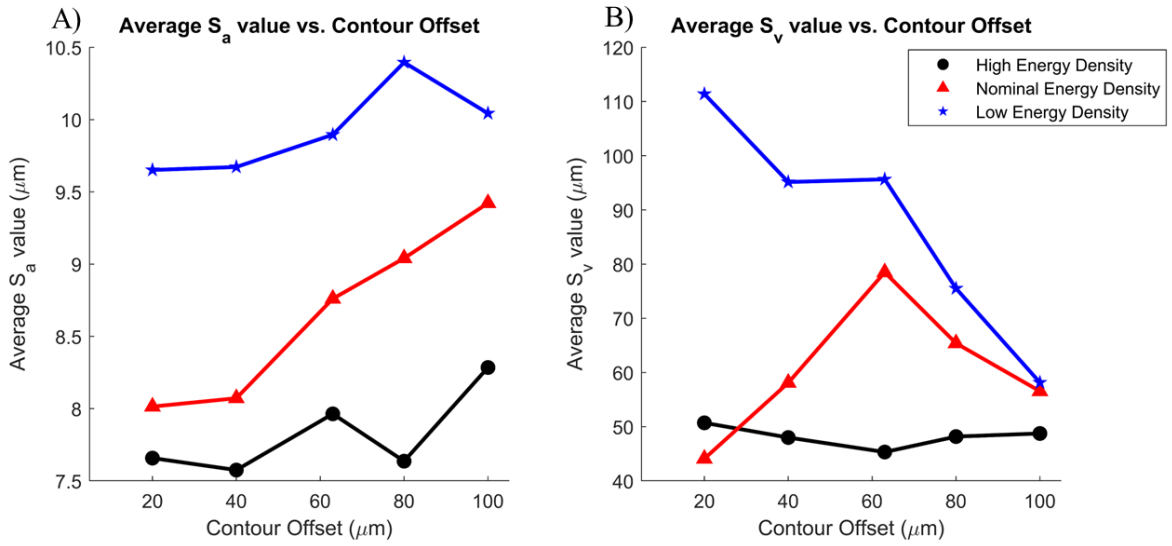

Figure 6: Contour offset vs. measured roughness for the three different melt pool sizes. Figure 6A shows the relationship between the average of all S_a measurements vs contour offset. Figure 6B shows the relationship between the average of all S_v measurements vs contour offset.

Images taken with the SEM show three factors that increased surface roughness. Partially adhered powder particles, spatter, and bulging melt tracks. Qualitatively, the number of powder particles adhered to the surface increased with the increase in contour offset, shown in Figure 7. The increase in powder particles can be attributed to the additional heat in the outer contour when it is scanned, partially adhering more powder. When the bulk and the outer contour are closer

together (increased contour offset), residual heat from the bulk scan can affect the outer contour [15]. The size of the weld tracks also increased, as shown in Figure 7. While this could be seen with the naked eye, the limited size of the SEM makes it difficult to picture. However, the visibility of these marks can still be seen between the two images.

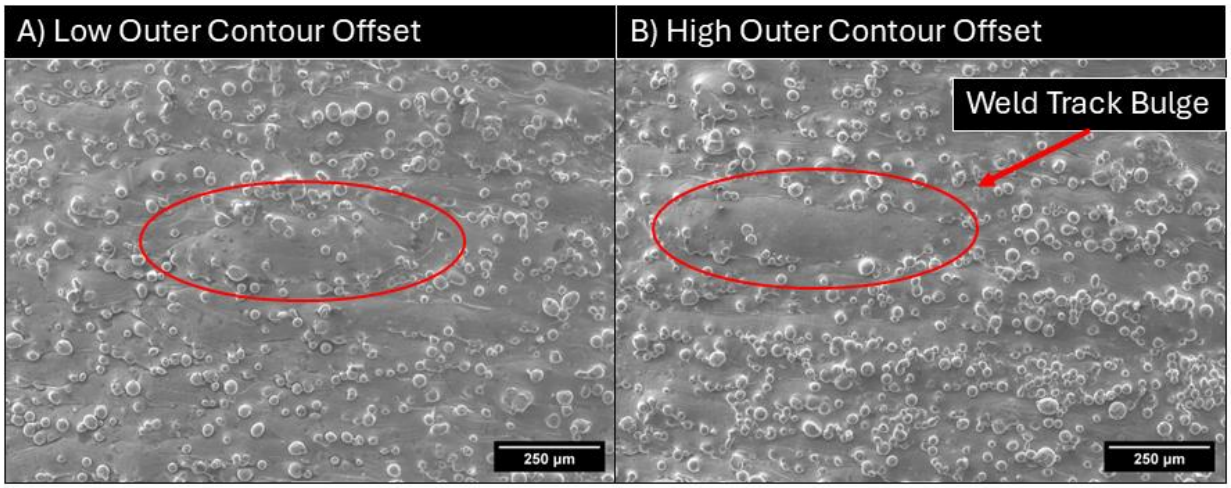

Figure 7: SEM images of the spiral track across the build height as contour offset increases. Both samples have the smallest melt pool size, to see the effect of changing only the outer contour offset. Figure 7A depicts the lowest offset tested (Sample 51) and Figure 7B depicts the highest offset used (Sample 55). Circled in red are weld tracks, which shows the larger height and size of the weld tracks in Figure 7b.

Figure 8 shows two SEM images comparing how the nominal sample compares to the sample that had the lowest measured S_a value. The overall primary surface of the sample is smoother, additionally with fewer partially adhered powder particles, resulting in a lower measured roughness.

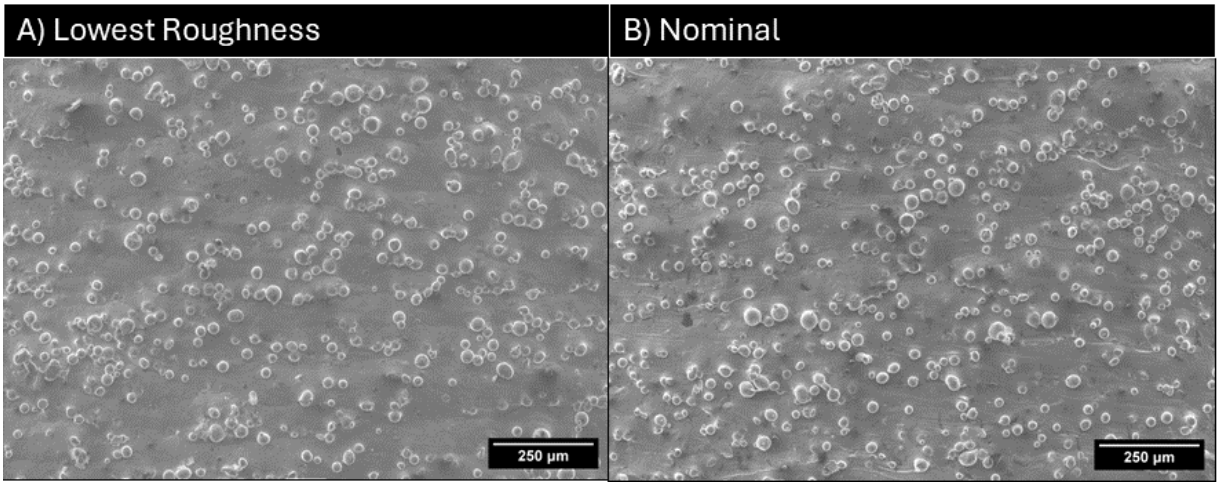

Figure 8: SEM images comparing the sample with the lowest average S_a measurement on all sides (Sample 42) vs. the nominal sample (Sample 48).

In general, the surface roughness was measured to be highest on the side facing away from the gas flow. The surface roughness was measured to be lowest on the numbered side which faced

towards the laser. Cuts were placed along the direction of the gas flow compared to the direction of the laser incident angle to inspect the contours for the highest roughness.

3.2. Sub-Surface Defect Analysis

Figure 9 below shows are images of etched sample cross sections. The minimum, maximum and nominal values of contour offset as well as the three melt pool sizes were included in the figure. Each sample was imaged on the contour facing away from the direction of the gas flow.

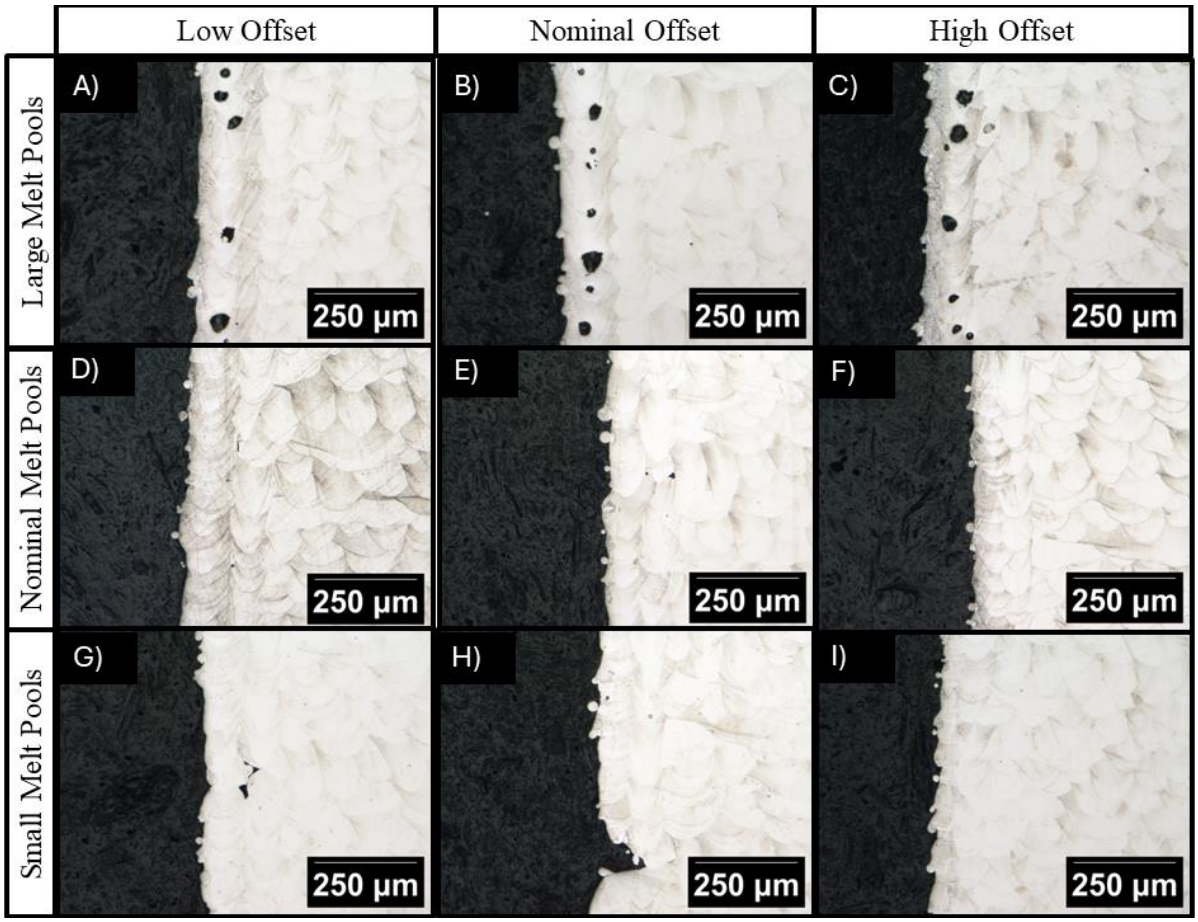

Figure 9: Etched samples of varying melt pool sizes and outer contour offsets. The low offset value pictured is 20 µm, the nominal offset value pictured is 63 µm, and the high offset value pictured is 100 µm. The build direction is vertical in the images.

Figure 9E is the nominal sample. It shows minimal sub-surface porosity with a relatively consistent surface finish. The pores that are shown are small and not consistent across the cross section. Figure 9D decreases the contour offset, bringing the contour further form the bulk. This results in more lack-of-fusion pores being present in between the outer and inner contour scans. Increasing the offset, as shown in Figure 9F, eliminates the sub-surface porosity and overlays the outer contour more on top of the inner contour scan.

Samples with a large melt pool showed high amounts of keyhole porosity, but a smoother outer surface. Shown in Figure 9A, Figure 9B, and Figure 9C above, there was minimal lack-of-fusion porosity, even with the lowest contour offset. A larger outer contour size can also be seen because of the larger melt pool.

The smallest melt pool size, shown in Figure 9G, Figure 9G, and Figure 9I above, produced no keyhole pores but had more sub-contour lack-of-fusion porosity at lower contour offsets (Figure 9G) than the nominal processing parameter samples. Figure 9H shows no porosity at the nominal offset but has a large surface defect shown. This sample (Sample 53) had several other instances of similar defects as well, possibly because of instability in the connection of the contour to the bulk material. The small melt pool requires more outer contour offset to reduce sub-surface porosity but is also more prone to surface defects.

3.3. Dimensional Accuracy

The diameter of the samples has a linear relationship with the value of contour offset. Shown in Figure 10 below, as the offset increases, the diameter of the sample decreases. All three melt pool sizes have similar slopes, but different y-intercepts. A larger melt pool size increases the overall size of the bar if the scan path placements are identical, because the scan path is placed at the middle of the melt pool. So, a larger melt pool width will increase the overall size of the part.

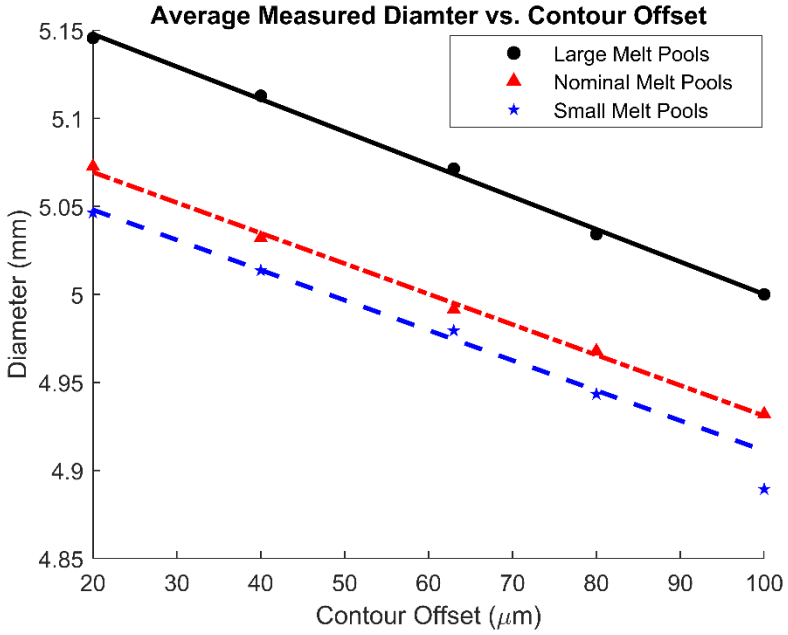

Figure 10: Relationship between measured diameter and contour offset for the three different melt pool sizes.

4. Conclusion

This work observed the effects of changing the outer contour pass' offset from the CAD geometry. The data collected and analyzed in this experiment lead to the following conclusions:

- Surface roughness of as-built parts in 316L stainless steel improves as melt pool size increases.
- As the outer contour pass is pushed further away from the CAD model's boundary by increasing the contour offset, the average surface roughness increases.
- Larger melt pool sizes can lead to keyhole porosity being formed within the contour passes.
- Moving the contour away from the bulk by decreasing the contour offset, leads to lack of fusion defects between the inner and outer contour.
- Contour offset interacts closely with the final measured dimensions of a part and overall offsets must be used to tune parameter sets for more dimensionally accurate parts to account for the size of the outer contour's melt pool.

References

[1] S. Sun, M. Brandt, and M. Easton, "Powder bed fusion processes: An overview", Accessed: Jun. 17, 2024. [Online]. Available: https://doi.org/10.1016/B978-0-08-100433-3.00002-6

[2] C. de Formanoir *et al.*, "Increasing the productivity of laser powder bed fusion: Influence of the *hull-bulk* strategy on part quality, microstructure and mechanical performance of Ti-6Al-4V," *Additive Manufacturing*, vol. 33, p. 101129, May 2020, doi: 10.1016/j.addma.2020.101129.

[3] P. Karimi, C. Schnur, E. Sadeghi, and J. Andersson, "Contour design to improve topographical and microstructural characteristics of Alloy 718 manufactured by electron beam-powder bed fusion technique," *Additive Manufacturing*, vol. 32, p. 101014, Mar. 2020, doi: 10.1016/j.addma.2019.101014.

[4] T. Reiber, J. Rüdesheim, M. Weigold, E. Abele, J. Musekamp, and M. Oechsner, "Influence of contour scans on surface roughness and pore formation using Scalmalloy® manufactured by laser powder bed fusion (PBF-LB)," *Materialwissenschaft und Werkstofftechnik*, vol. 52, no. 4, pp. 468–481, 2021, doi: 10.1002/mawe.202000287.

[5] H. Karimialavijeh, M. Ghasri-Khouzani, A. Das, M. Pröebstle, and É. Martin, "Effect of laser contour scan parameters on fatigue performance of A20X fabricated by laser powder bed fusion," *International Journal of Fatigue*, vol. 175, p. 107775, Oct. 2023, doi: 10.1016/j.ijfatigue.2023.107775.

[6] D. Bourell *et al.*, "Materials for additive manufacturing," *CIRP Annals*, vol. 66, no. 2, pp. 659–681, Jan. 2017, doi: 10.1016/j.cirp.2017.05.009.

[7] T. Yang *et al.*, "Laser powder bed fusion of AlSi10Mg: Influence of energy intensities on spatter and porosity evolution, microstructure and mechanical properties," *Journal of Alloys and Compounds*, vol. 849, p. 156300, Dec. 2020, doi: 10.1016/j.jallcom.2020.156300.

[8] J. Gockel, L. Sheridan, B. Koerper, and B. Whip, "The influence of additive manufacturing processing parameters on surface roughness and fatigue life," *International Journal of Fatigue*, vol. 124, pp. 380–388, Jul. 2019, doi: 10.1016/j.ijfatigue.2019.03.025.

[9] J. C. Snyder and K. A. Thole, “Understanding Laser Powder Bed Fusion Surface Roughness,” *Journal of Manufacturing Science and Engineering*, vol. 142, no. 071003, May 2020, doi: 10.1115/1.4046504.

[10] C. Guo *et al.*, “Effect of processing parameters on surface roughness, porosity and cracking of as-built IN738LC parts fabricated by laser powder bed fusion,” *Journal of Materials Processing Technology*, vol. 285, p. 116788, Nov. 2020, doi: 10.1016/j.jmatprotec.2020.116788.

[11] A. Jones, M. Leary, S. Bateman, and M. Easton, “Effect of surface geometry on laser powder bed fusion defects,” *Journal of Materials Processing Technology*, vol. 296, p. 117179, Oct. 2021, doi: 10.1016/j.jmatprotec.2021.117179.

[12] S. Rott, A. Ladewig, K. Friedberger, J. Casper, M. Full, and J. H. Schleifenbaum, “Surface roughness in laser powder bed fusion – Interdependency of surface orientation and laser incidence,” *Additive Manufacturing*, vol. 36, p. 101437, Dec. 2020, doi: 10.1016/j.addma.2020.101437.

[13] Z. Liu *et al.*, “Flow field analysis for multilaser powder bed fusion and the influence of gas flow distribution on parts quality,” *Rapid Prototyping Journal*, vol. 28, no. 9, pp. 1706–1716, Jan. 2022, doi: 10.1108/RPJ-12-2021-0351.

[14] “OmniSurf3D - Digital Metrology.” Accessed: Jun. 25, 2024. [Online]. Available: https://digitalmetrology.com/solution/omnisurf3d/

[15] S. Shrestha and K. Chou, “Residual Heat Effect on the Melt Pool Geometry during the Laser Powder Bed Fusion Process,” *Journal of Manufacturing and Materials Processing*, vol. 6, no. 6, Art. no. 6, Dec. 2022, doi: 10.3390/jmmp6060153.